Journal of Materials Chemistry A

ROYAL SOCIETY OF CHEMISTRY

PAPER

View Article Online
View Journal

Cite this: DOI: 10.1039/d6ta00467a

Creating percolating Li diffusion pathways *via* Ge substitution enables the fabrication of thick-electrode oxide all-solid-state batteries

Seungjun Woo,†[a] Junhyung Park, †[a] Donghun Lee,[a] Woojin Song,[a] Zhan Yu,[b] Hong Zhu,[b] Maxim Avdeev,[cd] Nicolas Dupré[e] and Byoungwoo Kang *[a]

Even though oxide solid electrolytes (SEs) have several advantages such as high chemical/thermal stability over conventional liquid electrolytes, their low ionic conductivity and difficult integration during cell fabrication hinder practical application. Here, the Li ionic conductivity of the LISICON (lithium super ionic conductor)-type SE is enhanced by substitution of Ge, achieving conductivity approximately 5 times higher than that of the unsubstituted. The Ge substitution can not only increase the concentration of Li but also enhance partial occupancies of Li at specific sites, enabling additional Li diffusion pathways and thereby leading to high ionic conductivity. Surprisingly, unlike other Ge-based solid electrolytes, the Ge-substituted LISICON-type SE exhibits excellent wetting behavior with Li metal and co-sintering capability with high-capacity cathodes even at temperatures above 700 °C. The increased Li ionic conductivity and excellent co-sintering capability enable the fabrication of an all-solid-state battery (ASSB) with an ultra-thick composite electrode (~140 μm), which delivers high electrochemical activity/reversibility at room temperature without external pressure. These findings clearly demonstrate that the LISICON-type SE with enhanced Li ionic conductivity provides a completely novel strategy for achieving high energy density in ASSBs and offers a promising route toward practical application of oxide-based SEs in high-energy density ASSBs.

Received 17th January 2026
Accepted 23rd April 2026

DOI: 10.1039/d6ta00467a

rsc.li/materials-a

1 Introduction

Li-ion batteries (LIBs) with liquid electrolytes have fundamental limitations in increasing energy density due to the narrow electrochemical window and in guaranteeing thermal safety due to the flammable properties of the organic liquid electrolytes.[1,2] Since safety measures that will increase an inactive component in a battery package are used to minimize the safety problems, the energy density of the battery package can be sacrificed. Therefore, the liquid electrolytes should be replaced for further improving safety and increasing energy density in LIBs.[3] Among several promising next-generation battery technologies, an all-solid-state battery (ASSB) with an oxide-based solid electrolyte (SE) has been of great interest because it has a wider electrochemical window and superior thermal safety than liquid electrolytes, sulfide-based SEs, and polymer-based SEs.[4,5] The use of the oxide-based SEs has several advantages over the liquid ones in addition to superior thermal stability. They do not have any leakage or vaporization problem, and can easily make bipolar stacked cells leading to a sharp increase in the volumetric energy density unlike the liquid electrolytes.[6] However, the oxide-based SEs still require a high-temperature sintering process to integrate three components such as the cathode, anode, and SE in the ASSB process and should have much improved Li ionic conductivity and Li metal wettability.[7] During the co-sintering process at high temperature (>700 °C), most of the oxide-based SEs such as garnet-type ($Li_7La_3Zr_2O_{12}$)[8–10] and NASICON-type ($Li_{1+x}Al_xTi(Ge)_{2-x}(PO_4)_3$)[11,12] SEs chemically react with active electrode materials resulting in the loss of their electrochemical activity as a battery material.[13–15] Therefore, it is a quite challenging issue to integrate composite electrodes with oxide-based SEs for constructing ASSBs.[16,17] With respect to the co-sintering capability, we recently reported that a LISICON-type oxide SE (LSPO-$Li_{3.5}Si_{0.5}P_{0.5}O_4$) barely shows any chemical reaction with high-capacity Ni-based layered oxides even at 900 °C, and has excellent stability and wettability with Li metal.[18] These intriguing properties allow negligible interfacial resistance with both electrodes and enable seamless Li transport at the interface even without external

[a]Department of Materials Science and Engineering, Pohang University of Science and Technology (POSTECH), Pohang, 37673, Republic of Korea
[b]University of Michigan, Shanghai Jiao Tong University Joint Institute, Shanghai Jiao Tong University, 800 Dongchuan Road, Shanghai 200240, China
[c]Australian Nuclear Science and Technology Organisation (ANSTO), New Illawarra Road, Lucas Heights, NSW 2234, Australia
[d]School of Chemistry, The University of Sydney, City Road, Darlington, NSW 2006, Australia
[e]Université de Nantes, Institut des Materiaux Jean Rouxel (IMN), CNRS UMR 6502, 2 rue de la Houssiniere, BP 32229, 44322 Nantes Cedex 3, France
† Equal contribution.

pressure. Even though these fascinating advantages of the LSPO SE can enable the integration of ASSBs with high-capacity cathode materials, LSPO SEs still suffer from poor Li ionic conductivity ($\sim 10^{-6}$ S cm^{-1})[19] compared to the garnet-type SEs and NASICON-type SEs. To practically use the oxide-based ASSBs, the poor Li ionic conductivity should be improved. Many efforts have gone to increase the Li ionic conductivity in LSPO SEs. For example, doping with elements such as Ga or others is used to enhance ionic conductivity,[20,21] and recent studies have focused on forming solid solutions among multiple phases with the LISICON structure.[22–24] Furthermore, Ceder *et al.*[25] recently reported that the ionic conductivity in SEs can be increased by controlling the local distortions, which enable the overlap of site energy distributions for Li ions, thereby facilitating the formation of a percolation network with low activation energy. The multi-cation doping or substitution in SEs can increase local distortion leading to an increase in ionic conductivity.[25,26] In SEs, the Li ionic conductivity can be improved by doping (or substitution) and the change in the distribution of Li in Li sites.

The LISICON (LSPO) structure has six types of Li sites, four tetrahedral sites and two octahedral sites but most of the Li ions mainly sit in the four tetrahedral sites.[19] As a result, the Li ions between the Li sites are not continuously connected leading to poor Li connectivity. To increase the Li ionic conductivity, the connectivity of Li ions between sites should be improved. Here, through an experimental and computational combined approach, we report that the Li ionic conductivity of the LSPO SE can be substantially increased by Ge substitution instead of equal amounts of P and Si. The Ge substituted LSPO sample shows Li ionic conductivity of $\sim 2.5 \times 10^{-5}$ S cm^{-1} which is $\sim$5 times higher than that of the pristine one. The increase can be ascribed to the effects of Ge substitution which can not only increase the amount of available Li concentration but also cause an increase in the partial occupancy of Li sites, which are close to Ge. The substitution of P^{5+}/Si^{4+} by Ge^{4+} modifies the charge balance, and the available Li concentration increases accordingly from 3.5 to 3.75 mol. Furthermore, the Ge substitution substantially affects the occupancies and the distribution of Li in Li sites. Firstly, the Li amount increased by Ge substitution can be preferentially incorporated in specific Li sites such as the octahedral sites which are not well occupied in the pristine one. This increased occupancy in octahedral sites can form continuous connectivity of Li between Li tetrahedral sites and octahedral sites. Secondly, the presence of Ge as an MO_4 frame can increase the partial occupancy of Li in Li sites which are close to Ge. As a result, Ge substitution substantially improves the poor connectivity of Li ion between Li sites in addition to the increase in the Li concentration and, thereby can increase the Li ionic conductivity. Furthermore, the Ge substituted LSPO sample still maintains superior compatibility with high-capacity Ni-rich layered oxides without any chemical reactions even with the co-sintering process at 700 °C and good wettability with Li metal at 250 °C even though it has a large amount of Ge in the bulk. This good Li metal wettability of the Ge-substituted LSPO sample is quite different from other Ge-substituted oxide-based SEs such as NASICON-type $Li_{1.5}Al_{0.5}Ge_{1.5}(PO_4)_3$ (LAGP) which undergoes a severe chemical reaction and thermal runaway with Li metal. As a result, the Ge-substituted SE based ASSB can achieve high capacity with much enhanced kinetics at room temperature. Furthermore, the improved Li ionic conductivity and the co-sintering capability in the Ge-substituted LISICON-type SE can enable the realization of a thick composite electrode ($\sim$140 μm) that can substantially increase energy density. The Ge-substituted SE based ASSB which has a thick composite electrode and Li metal can reversibly achieve high energy density even at room temperature without any external pressure. This result demonstrates that the LISICON-type SE-based ASSB will employ a totally different strategy from conventional ones to further increase the energy density even without any external pressure.[27] Considering the superior capabilities of the LISICON-type SE for achieving high energy density, the results and the demonstration will pave the way for the practical use of the oxide-based ASSBs with high-energy density.

2 Results & discussion

2.1 Structural characterization of samples with different amounts of Ge substitution

To enhance the Li ionic conductivity, different amounts of Ge were substituted for equal amounts of P and Si in LSPO ($Li_{3.5}Si_{0.5}P_{0.5}O_4$), and Ge-substituted samples ($Li_{(3.5+x/2)}(SiP)_{(0.5-x/2)}Ge_xO_4$, x = 0.1, 0.2, 0.3, 0.4, 0.5) were synthesized at 700 °C for 3 hours under an oxygen atmosphere. It should be noted that increasing the Ge content linearly increases the Li content to maintain charge balance. The Ge-substituted samples were labeled according to the amount of Ge substitution. For example, the Ge-substituted LSPO sample with 0.5 mol of Ge was labelled as Ge50. The crystal structures of the samples were characterized by XRD and NPD measurements. XRD patterns in Fig. 1a show that all samples have an orthorhombic structure like the LISICON structure (γ-Li_3PO_4 structure) of the LSPO ($Li_{3.5}Si_{0.5}P_{0.5}O_4$) without any impurities even at high Ge content. The inset in Fig. 1a shows that the (012) and (110) peaks shift linearly toward lower angles with increasing Ge amount, indicating lattice expansion due to the larger size of GeO_4 compared to SiO_4 and PO_4. This indirectly confirms that the Ge can be incorporated into the bulk structure. The refinement results in Fig. 1b clearly show that the volumes of the Ge-substituted samples linearly increase with the Ge incorporation amount indicating that the Ge-substituted samples obey the Vegard's law. This further confirms that the Ge element is substituted into the bulk of the LSPO. Neutron powder diffraction (NPD) measurements were carried out in the samples to understand the changes in the M–O bond length. NPD patterns in Fig. 1c and d show that the LSPO and Ge50 sample have the same structure without any impurity phases. The Rietveld refinements of the NPD patterns show that the average M–O bond lengths of the Ge-substituted samples linearly increase with the amount of Ge. This result indicates that the linear increase in the volumes can be ascribed to the increase in the Ge–O and further confirms that the Ge element is well substituted into the bulk structure. The Ge-substituted samples have similar particle morphology and size to those of

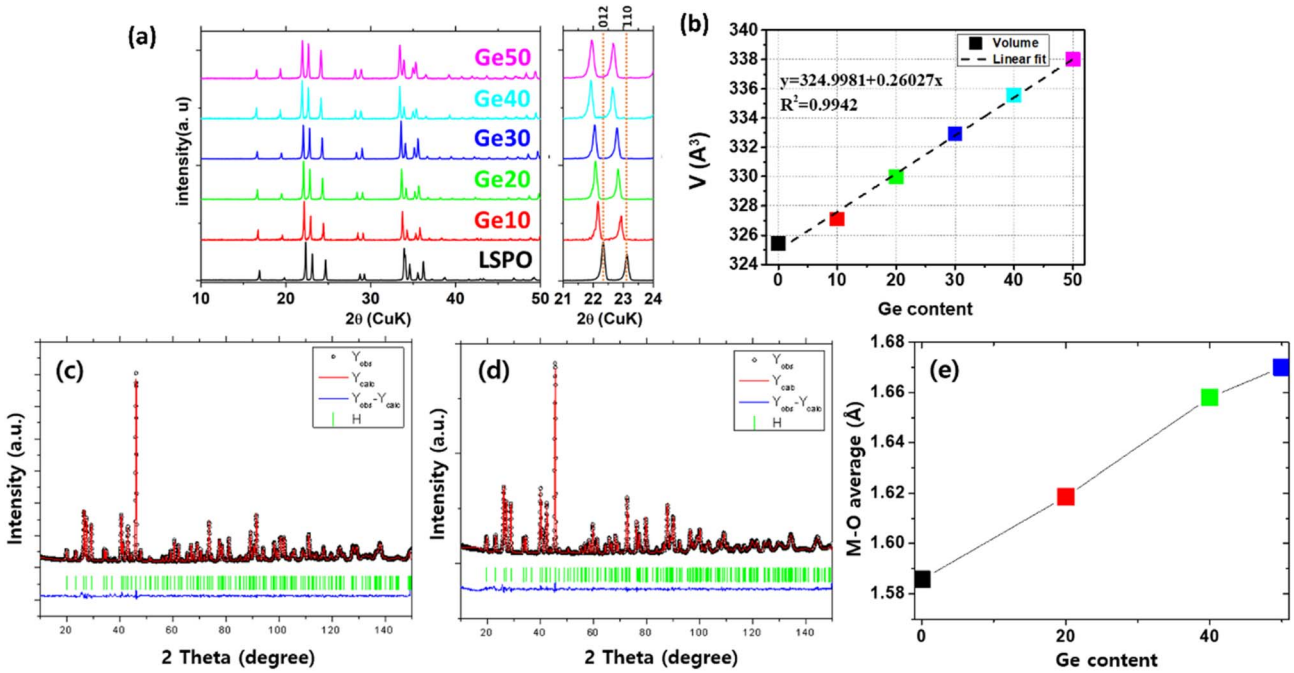

Fig. 1 Structural characteristics of the samples with different amounts of Ge (a) XRD patterns, (b) volume changes with increasing Ge content. Neutron powder diffraction (NPD) pattern of (c) LSPO, (d) Ge50, and (e) average M–O bond lengths with the Ge substitution.

the bare sample (SI Fig. S1), and all samples exhibit comparable high relative densities (>97%, SI Table S1).

2.2 The increase in the Li ionic conductivity in the Ge-substituted samples according to the Ge substitution

To understand the electrical properties of the Ge-substituted samples, electrochemical impedance spectroscopy (EIS) measurements were performed at room temperature. Fig. 2a shows Nyquist plots of the samples with different amounts of Ge substitution. All samples have one semi-circle without a tailing behavior. One semi-circle can imply that the bulk and grain boundary resistance are not distinguished at room temperature and total resistance can be measured. The total resistances, which can be evaluated by the size of the first semi-circle, decrease as the Ge substitution increases. The Li ionic conductivity of the samples was calculated using the total resistance and the geometric factor of the sample pellet. Fig. 2b clearly shows that the Li ionic conductivity of the Ge-substituted samples almost linearly increases according to the amount of Ge. The bare LSPO has $\sim 5.5 \times 10^{-6}$ S cm^{-1} whereas the Ge50 sample has $\sim 2.5 \times 10^{-5}$ S cm^{-1}, which is $\sim$5 times higher than the bare sample. Given that the Ge element is incorporated into

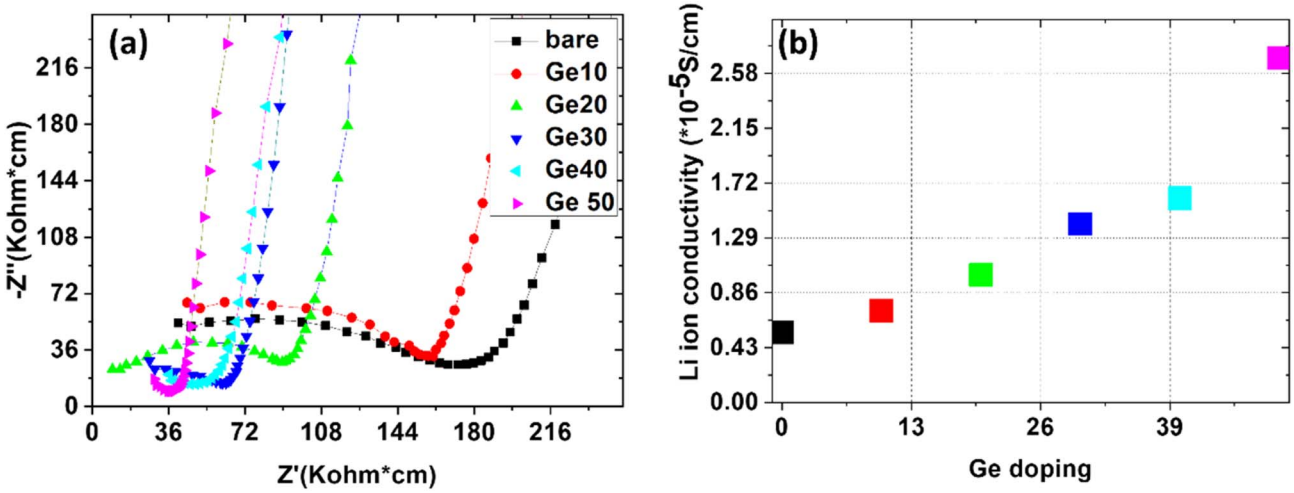

Fig. 2 Electrical properties of the samples with different amounts of Ge (a) Nyquist plot (1 MHz ~0.1 Hz). (b) Total Li ionic conductivities of the samples at RT.

the bulk as shown in Fig. 1, the increase in the Li ionic conductivity is related to the effects of the Ge substitution, such as the increased Li amount and the change in the volume. Temperature-dependent ionic conductivity measurements were performed for bare LSPO, Ge30, and Ge50 (SI Fig. S2). The activation energies show a slight decrease with increasing Ge content, supporting enhanced Li ionic conductivity upon Ge substitution.

To quantitatively characterize the Li occupancy in Li sites, Li distributions in the samples were refined by using NPD measurements. Structural information of the samples was refined by the Rietveld refinement with the LISICON structure, γ-Li_3PO_4-type $Li_{3.5}Si_{0.5}P_{0.5}O_4$. In the LISICON structure, there are 6 different Li sites that are labeled as Li1 ~ 6. Among them, four Li atoms sit in a tetrahedral site (LiO_4; Li1, 2, 3, and 5) and the other two Li atoms sit in an octahedral site (LiO_6; Li4, 6). The refinement results based on the NPD measurements are shown in SI Fig. S3, and the details are summarized in SI Table S2. NPD refinement results clearly show that the total amount of Li in the Ge-substituted samples increases according to the amount

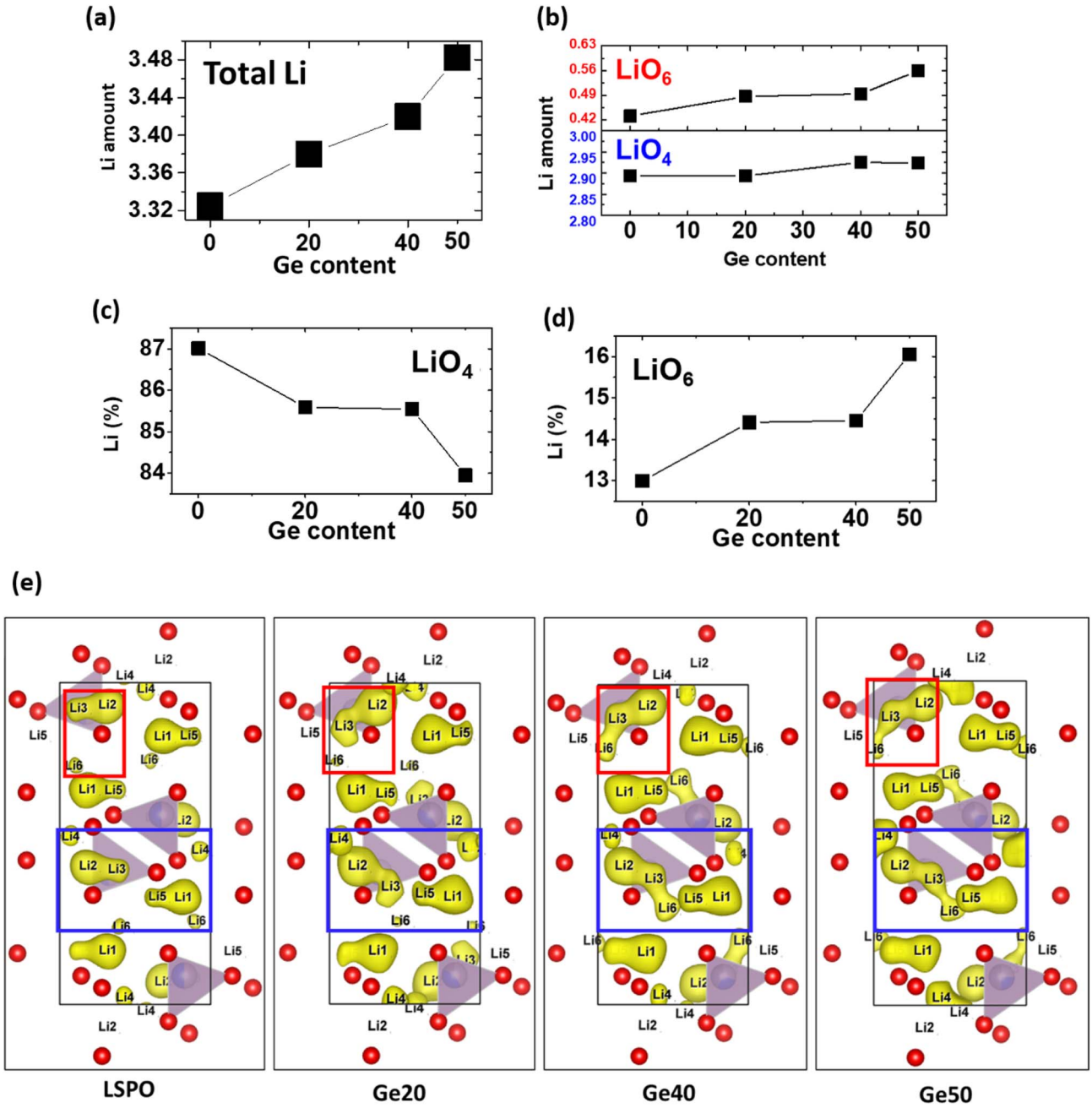

Fig. 3 Rietveld refinement results of the samples based on neutron powder diffraction: (a) total amount of Li; (b) change of Li amount in LiO_4 (tetrahedral site) and LiO_6 (octahedral site) and the change in the ratio of (c) LiO_4 and (d) LiO_6. (e) The distribution of the Li ion density in the LISICON structure in the samples by using the MEM (maximum entropy method).

of Ge (Fig. 3a) as expected. This further confirms that Ge is substituted into the bulk and then the charge balance is mainly satisfied by the increase in the Li amount. Furthermore, the Ge substitution strongly affects the occupancy and distribution of Li in the Li sites in Fig. 3b. In the bare sample, most of the Li atoms in the LISICON structure occupy the tetrahedral sites (LiO_4), with a small portion of Li atoms in the octahedral sites (LiO_6). As the amount of Ge substituted increases, the Li occupancies in the tetrahedral and octahedral sites change. Fig. 3b shows that the amount of Li in tetrahedral LiO_4 sites barely changes but that in octahedral LiO_6 sites increases according to the Ge amount. Given that the amount of Li in the Ge-substituted LSPO samples increases with the Ge amount due to the charge balance, the increased amount of Li can mainly go to the octahedral LiO_6 sites rather than the tetrahedral LiO_4 sites. This indicates that the Ge substitution can not only increase the amount of Li but also can affect the occupancy of Li in the Li sites. Furthermore, the fraction of the Li in the octahedral LiO_6 sites continuously increases with increasing Ge content, whereas the fraction of the Li in tetrahedral LiO_4 sites slightly decreases, as shown in Fig. 3c and d. This indicates that the distribution of Li in the two Li sites is changed by the substitution of Ge into the LISICON structure. The increase and change in the distribution and occupancy of Li in the Li sites can improve the connectivity of the Li between the two Li sites resulting in additional formation of the Li percolation pathway. Ge substitution can not only increase the available Li amount but also enhance the occupancy of the Li octahedral sites and the distribution of Li between Li sites resulting in the increase in the connectivity of Li sites that can form the additional Li diffusion pathway.

The maximum entropy method (MEM) was employed to reconstruct the nuclear density distribution of Li from the NPD data, enabling the three-dimensional visualization of Li ion spatial distributions. Notably, MEM provides detailed insight into the delocalized and anisotropic nature of Li around crystallographic sites, reflecting both statistical occupancy and potential diffusion pathways within the structure. Fig. 3e shows the visualization of the Li density distribution in the Li sites in the samples. The red circle represents the oxygen (O) element, and the purple tetrahedron represents the polyanion (MO_4, M = Si^{4+}, P^{5+}, and Ge^{4+}). The yellow space represents the nuclear density of ^{7}Li. As the Ge substitution increases, the density of Li in the octahedral sites such as Li4 and Li6 gradually increases. As a result, this increase strongly affects the connectivity of Li ions between Li sites in the structure. For example, the connectivity of Li6–Li3 in the red rectangle box in Fig. 3e is substantially improved with the amount of Ge and thereby, an additional connected network of Li could be created. The nuclear density of Li ions in Li2 and Li3 sites also can be broadened. This can help to overlap the Li density between sites and thereby could increase the connectivity of Li in the structure. Furthermore, the connectivity of the Li1–Li5–Li6–Li3–Li2 pathway in the blue rectangle box in Fig. 3e can be improved by the increase in the Ge substitution. As a result, the Ge substitution substantially improves the connectivity of the percolation network of Li in the structure. Consequently, the Ge substitution can not only increase the available Li amount, which strongly affects the occupancy of the octahedral sites that are not occupied in the pristine one, but also affect the distribution of the Li in the sites, which can increase the possibility of the formation of the connected channel. These effects enable the increase in the Li ionic conductivity.

2.3 The change in the local environments of Li caused by the Ge substitution

To understand the effects of the Ge substitution on the Li local environments in the LISICON structure, ^{7}Li MAS (Magic Angle Spinning) NMR (Nuclear Magnetic Resonance) measurements were carried out in the samples. Given that the LISICON structure has two Li local environments such as the tetrahedral and octahedral sites, NMR results in Fig. 4a–c clearly show that all samples including the Ge-substituted ones have similar Li environments. This indicates that the Ge substitution does not create new Li environments in the structure. The Li in the Ge-substituted samples sits similarly in the tetrahedral sites (LiO_4) and octahedral sites (LiO_6). Only two peaks of Li in NMR data were identified: one is for the tetrahedral site and the other is for the octahedral site, which has a broader peak width than the tetrahedral site. The intensity of the NMR peak of Li in the samples decreases with increasing Ge content, even though the amount of Li increases. This indicates that the local environments of Li get broadened with the increase in the Ge amount. Fig. 4d shows the ratio of the Li sites obtained through ^{7}Li NMR in each sample. As the Ge amount increases from 0 to 40 mol%, the Li amount of the tetrahedral site gradually decreases while the Li concentration in the octahedral site gradually increases. This is consistent with the NPD refinement results. The decrease in the Li amount in the tetrahedral sites indicates that the distribution of Li in the LISICON structure is changed due to the Ge substitution. Given that the Li amount can linearly increase according to the Ge substitution due to a charge balance, the change in the distribution of Li can be caused by not only the presence of Ge instead of Si and P but also the increased Li amount. As shown in Fig. 4e, FWHMs of the Li peaks in the samples substantially increase when the amount of Ge increases to 40% even though the amount of Li increases. This indicates that the incorporation of Ge can make Li local environments broad and disordered. As a result, the increased disordering of Li in the Ge-substituted samples can enhance the possibility of formation of the connectivity of the Li sites.

2.4 AIMD simulation results of the effects of the Ge substitution on Li distribution in the LISICON structure

Ab-Initio Molecular Dynamics (AIMD) simulations were conducted to investigate the effects of Ge substitution on the distribution of Li in Li sites and its local environments within the LISICON structure, and to understand the formation of conduction pathways. Fig. 5a shows that the occupancies of Li in the tetrahedral sites such as Li1, Li2, Li3, and Li5 sites remain similar even after the Ge substitution whereas the occupancies of the Li in the octahedral sites such as Li4 and Li6 sites increase significantly with the increasing Ge content. This

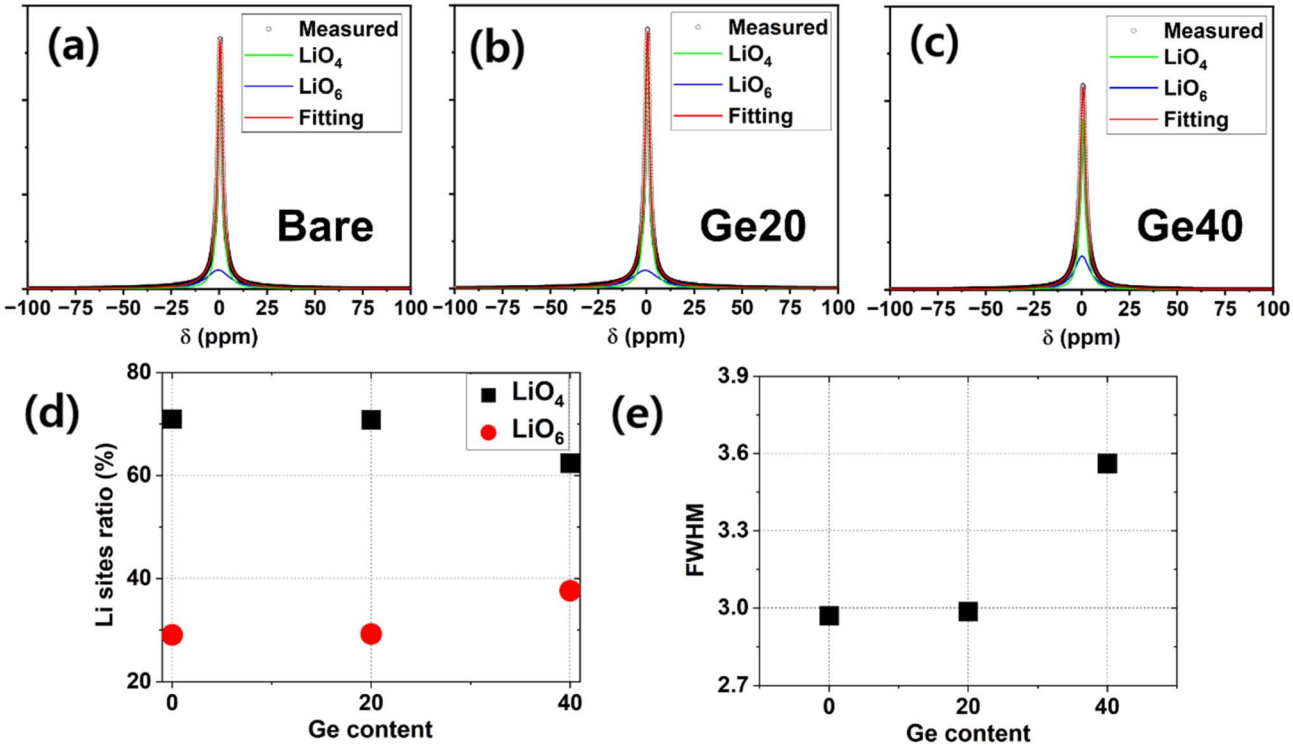

Fig. 4 ^{7}Li MAS (30 kHz) NMR results for the samples. (a) Bare, (b) Ge20, (c) Ge40. (d) The change in the fraction of Li in the samples depending on the Ge amount. (e) FWHM results of the Li NMR peak in the samples.

indicates that the Ge substitution substantially affects the change in the occupancy of the octahedral Li sites. This is consistent with the above MEM results *via* NPD measurements in Fig. 3e and NMR results. The Ge substitution leads to increased Li occupancy at octahedral sites that are mostly located near Ge atoms. Consequently, the increased occupancy in octahedral sites enables the additional Li ion diffusion pathway such as the Li6–Li1–Li4–Li1–Li6 pathway which is connected *via* the octahedral sites. This indicates that the presence of Ge instead of P and Si can strongly affect the surrounding local environments of Li within the LISICON structure partly due to the modulated Ge–O bond strength as shown in NPD data (Fig. 1e).

To visualize the effect of Ge substitution on the distribution of Li in the structure, and its impact on the Li diffusion pathway, the probability density distribution of Li calculated by

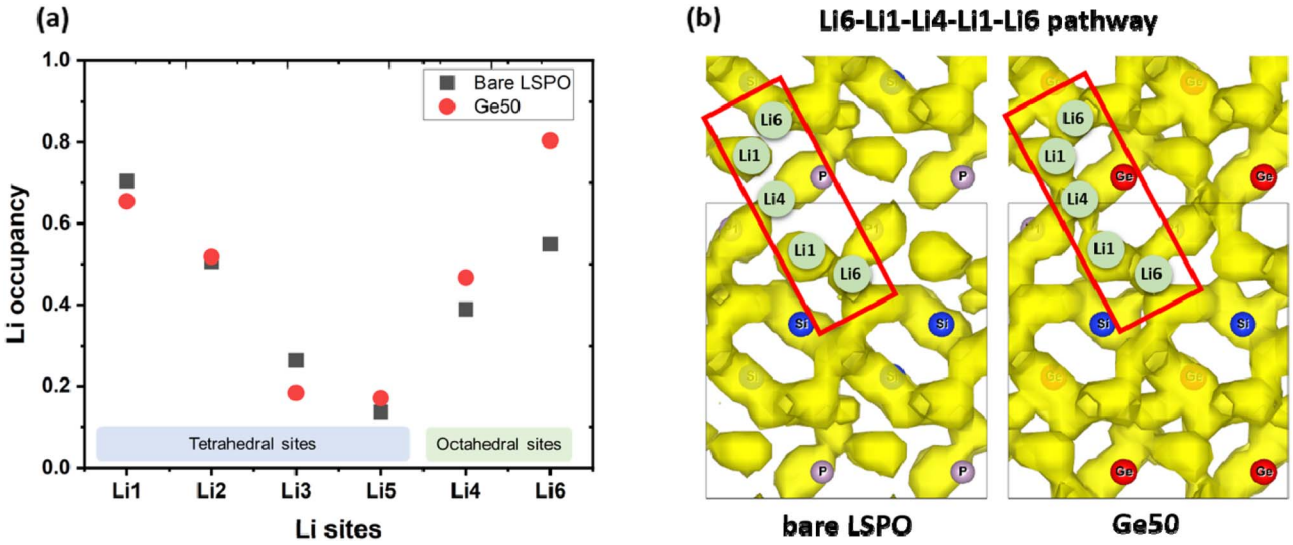

Fig. 5 AIMD simulation results of the samples with different amounts of Ge. (a) The occupation of Li in Li sites of bare LSPO and Ge50. (b) Calculated Li probability density distribution maps showing the formation of the Li percolation pathway in the LISICON structure.

the simulation results is plotted in Fig. 5b and SI Fig. S4. The density plots of Li clearly show that the Ge substitution can form additional Li diffusion pathways *via* the increase in the occupancy of the octahedral Li sites by expanding the connectivity of the nearby Li diffusion channels. In Fig. 5b, the Li6–Li1–Li4–Li1–Li6 pathway in the Ge50 sample, which does not have any connectivity in the bare sample, is formed resulting in the significant increase in the connectivity by the increased distribution probability of Li atoms in the two octahedral Li sites. As a result, the Li ionic conductivity in the Ge50 sample can be substantially increased due to the additional formation of Li diffusion channels caused by the effects of the Ge substitution, which affects the increase in the available Li amount and Li site distributions, especially the octahedral sites.

2.5 Superior compatible properties of the Ge-substituted samples with Li metal and the Ni-rich layered oxides

Unlike other oxide-based solid electrolytes, our previous study[18] clearly demonstrates that the LISICON-type LSPO SE can have superior compatibilities with high-capacity Ni-rich layered oxides and superior wetting behavior with Li metal resulting in a high energy density all-solid-state battery that reversibly operates at room temperature. However, the Ge element can cause a reaction with Li metal. For example, the NASICON-type $Li_{1.5}Al_{0.5}Ge_{1.5}(PO_4)_3$ (LAGP) SE shows a vigorous chemical reaction with Li metal due to the reduction of Ge, thereby causing severe thermal runaway above 250 °C.[11,28] Therefore, the Ge-substituted LSPO samples should be evaluated for their reactivity with the Li metal and high-capacity Ni electrode materials.

Experiments were conducted to find out the reactivity of the Ge-substituted LSPO sample with Li metal. A Li metal wetting experiment with the Ge50 pellet was carried out at 250 °C in the glovebox, which has low level of oxygen and H_2O. Fig. 6a shows that the Ge50 sample has a good wetting behavior with wetted Li metal like the bare LSPO sample which neither has any Ge nor undergoes any chemical reactions. The wetted Li metal can make excellent and uniform physical contact with the Ge50 pellet in Fig. 6b. The thickness of the wetted Li layer can be reduced to below 10 μm by wiping the pellet surface while the Li is in a molten state, as shown in SI Fig. S5. This is quite different Li metal wetting behavior from the NASICON-type LAGP SE which also has Ge element and shows severe thermal runaway in the middle of Li metal wetting.[11] The EIS results of a symmetric wetted Li metal cell in Fig. 6c and d show that the resistance of the Ge50 sample with the wetted Li metal is quite similar to that of the Ge50 sample with the Ag blocking electrode indicating that the interfacial resistance with the wetted Li metal can be almost negligible. The total resistance of the symmetric cell is ~2730 Ω, which is very close to the resistance of the Ge50 SE itself (~2660 Ω in Fig. 2). This indicates that the good Li metal wetting behavior of the Ge-substituted samples enables negligible interfacial resistance with Li metal. In addition, the electrochemical window of the Ge50 sample was measured and is shown in Fig. 6e to further investigate the electrochemical stability in the high voltage region. The electrochemical window of the Ge50 sample is almost ~7 V, which is quite similar to that of the bare LSPO. As a result, the Ge-substituted sample maintains superior Li metal wetting behavior even though it contains Ge element and a wide electrochemical window indicating that the Ge-substituted LSPO samples can use the wetted Li metal as an anode or

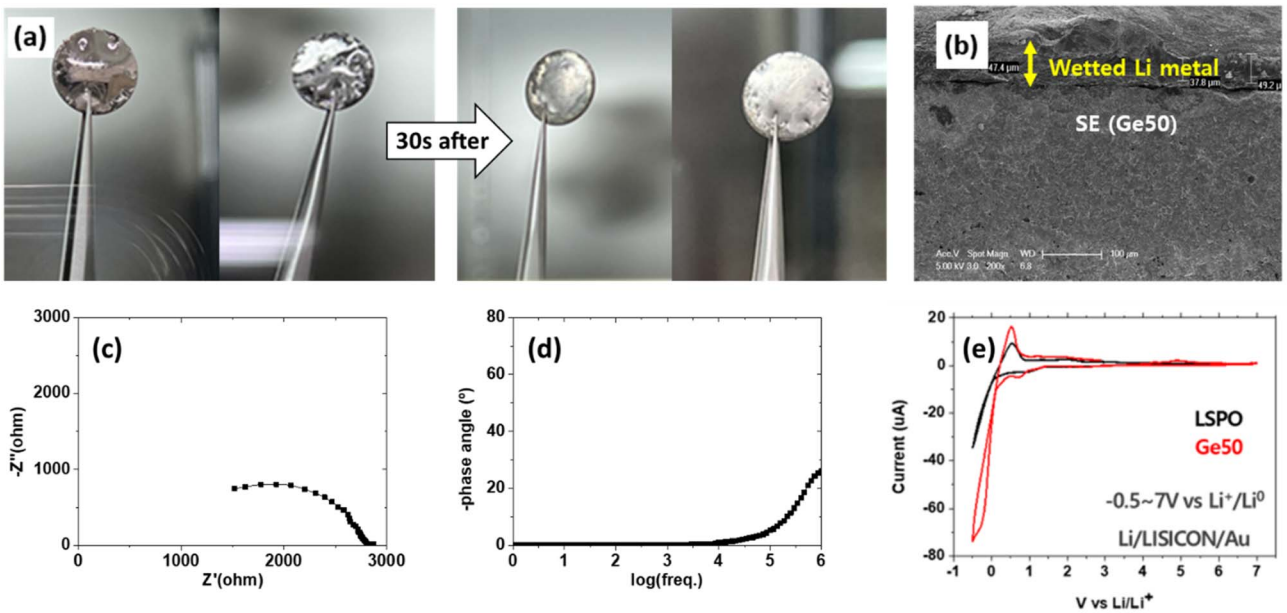

Fig. 6 (a) Images of the Ge50 pellet right after Li metal wetting at 250 °C and after 30 s; (b) cross-section SEM image of the Ge50 pellet with the wetted Li metal; (c) Nyquist plot and (d) Bode plot of the symmetric wetted Li|Ge50|wetted Li metal cell; (e) electrochemical potential window of Li|Ge50|Au.

a seed layer.[29] Time-dependent impedance measurements were performed using a Swagelok-type Li|SE|Li symmetric cell under a constant stack pressure to maintain physical contact (SI Fig. S6). Over 20 days, the bulk resistance remains unchanged, while the interfacial resistance gradually decreases, which is attributed to improved contact at the Li/SE interface rather than any electrochemical reaction.

Furthermore, the co-sintering capability of the Ge-substituted LSPO sample with high-capacity layered oxides such as high-capacity Ni layered oxides was evaluated. The single crystal $LiNi_{0.6}Mn_{0.2}Co_{0.2}O_2$ (NMC622) was co-sintered with the Ge50 sample at 700 °C for 3 hour under O_2. The XRD pattern in SI Fig. S7 shows that the Ge50 sample barely reacts with the NMC622 sample indicating it has quite good chemical stability even with the co-sintering process at high temperature. The lattice parameters determined by XRD measurements before and after the co-sintering process are listed in SI Table S3, corroborating that the LISICON-type SEs have high chemical stability with the NMC622 material. The Ni oxidation state and local structure from the XANES and EXAFS in SI Fig. S7 further confirm that the co-sintered NMC622 does not undergo any chemical reaction with the Ge50 SE. The co-sintered NMC622 sample with the Ge50 sample shows quite similar electrochemical behavior with the pristine NMC622 sample which is not co-sintered. This indicates that the co-sintering process can be applied to the Ge50 sample and high-capacity Ni layered oxides at high temperature to make intimate contact in the composite electrode for constructing a solid-state cell. It should be emphasized that the co-sintered composite electrode with the Ge50 SE does not need any external pressure for constructing a solid-state cell and operating it. Even though the Ge-substituted samples have certain amount of Ge element, they still have superior compatible properties such as superior Li metal wetting behavior and co-sintering processibility with high-capacity Ni layered oxides while having much higher Li ionic conductivity than the LSPO SE. Consequently, the Ge-substituted LSPO SE can achieve high energy density in making an all-solid-state battery by using Li metal and co-sintered high-capacity Ni-rich layered oxides even with better kinetics.

To evaluate the electrochemical properties of the ASSB which has the Ge50 SE, the ASSB was fabricated by using a co-sintering process at 700 °C under O_2 gas and the attached Li metal.[18] Two ASSBs were constructed. One is based on the LSPO SE with the NMC622 active material (0.76 mg cm^{-2} loading density) and the other is based on the Ge50 SE with the NMC622 active material (1.14 mg cm^{-2} loading density). In this work, Au was used as an electronic conductor in the cathode composite instead of conventional carbon additives due to the high-temperature co-sintering process (700 °C), where carbon is not stable. A relatively large amount of Au (1/3 vol%) was employed to ensure sufficient electronic conduction and to minimize limitations from electronic transport.

The EIS measurements of the two ASSBs in Fig. 7a show that the ASSB with the Ge50 SE has much lower total resistances than the ASSB with the LSPO SE. The ASSB with the LSPO SE has a resistance of ~22 kΩ, whereas the ASSB with the Ge50 SE has a resistance of ~5 kΩ. Both cells barely exhibit the interfacial resistance component, which can be ascribed to the well-formed interface between Li metal and the co-sintered composite electrode with the SE. The lowering of the total resistance in the ASSB with the Ge50 SE can be ascribed to the increased Li ionic conductivity in the Ge50 SE. In Fig. 7b, the LSPO-based ASSB shows high polarization and achieves a discharge capacity of 98 mAh g^{-1} at C/40, whereas the Ge50-based ASSB has much lower polarization and achieves a discharge capacity of 147 mAh g^{-1} at the same rate, which is 50% higher than the achieved capacity of the LSPO-based one. This can substantially increase the energy density of the Ge50-based ASSB. The sharply increased achievable capacity with reduced polarization is due to the increase in the Li ionic conductivity of the LSPO SE by Ge substitution that can help enhance the kinetics of the ASSB. However, the Ge-based ASSB still needs to significantly improve its electrochemical activity, which is lower than the 186 mAh g^{-1} discharge capacity achieved in liquid electrolytes. Considering that the Li ionic conductivity of SEs is critical for improving the electrochemical activity, the Li ionic conductivity of the LISICON-type SEs should be further improved.

Nevertheless, the cycling performance of the Ge50-based ASSB demonstrates its practical feasibility as a battery. As shown in Fig. 7c, the ASSB with the Ge50 SE can be stably operated at room temperature for 60 cycles at a current density of 16 mA g^{-1}, delivering a capacity retention of 89.3% with near-unity coulombic efficiency. The corresponding voltage–capacity profiles are provided in SI Fig. S8. These results indicate that despite the remaining limitations in electrochemical activity compared to liquid-electrolyte systems, the Ge50-based ASSB is capable of reliable operation under practical cycling conditions.

The increased Li ionic conductivity and the co-sintering capability of the Ge-substituted SE with high-capacity Ni layered oxides enable further increase of the achievable energy density by increasing the thickness of the composite electrode in ASSB cells. To evaluate the possibility of the Ge50 SE, a thick composite electrode that had a 36.80 mg cm^{-2} loading density of NCM622 and a thickness of ~140 μm was prepared by using a tape casting method with the co-sintering process at 700 °C (details in the Experimental section). The SEM cross-section of the thick electrode in Fig. 8a shows that the high loading thick electrode remains crack-free and intimately contacted with the Ge50 SE due to the co-sintering process at 700 °C. It should be noted that the co-sintering process at 700 °C uses the diffusion process, and thereby causes the intimate physical contact of the NCM622 with the Ge50 SE in the ultra-thick composite electrode even without any stacking pressure unlike a sulfide SE based ASSB. By using the ultra-thick composite cathode (~140 μm), the solid-state cell with the GE50 SE was constructed. Fig. 8b illustrates the pouch-type ASSB configuration, in which the Ge50 SE and the thick composite electrode are also integrated by the co-sintering process, and then Li metal was attached on the other side of the pellet. Fig. 8c and d show that the voltage curve of the pouch-type ASSB is quite similar to that of the cell with the liquid electrolyte. Even though the loading density of the active material substantially increases from

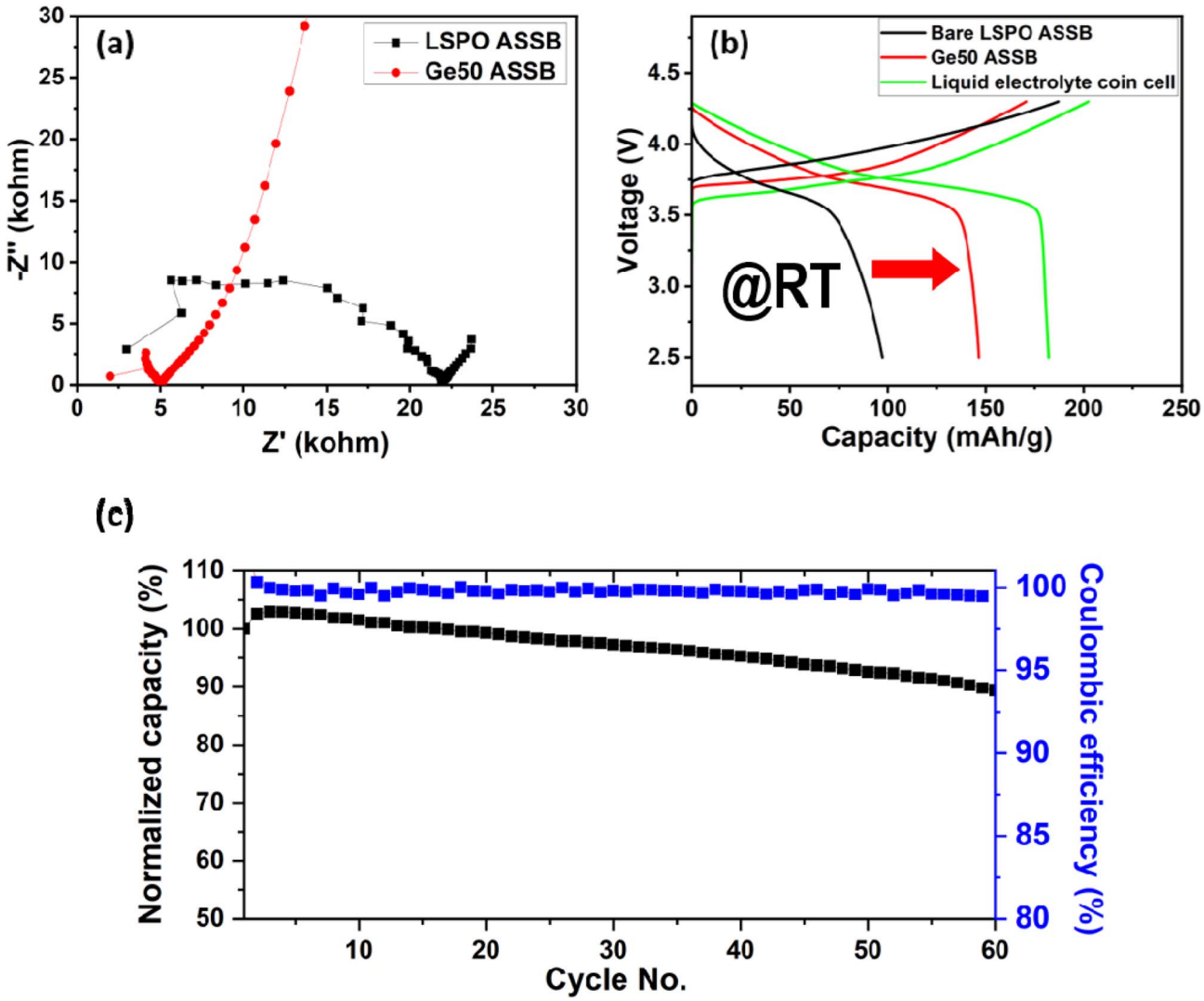

Fig. 7 (a) EIS results and (b) voltage curves of the ASSBs with Ge50 and the bare SE at room temperature (RT). The ASSB with the bare LSPO SE was fabricated with an NMC622 loading density of 0.78 mg cm^{-2}, while the ASSB with the Ge50 SE had 1.14 mg cm^{-2} of NMC622. Both cells were tested at C/40 current density under identical conditions. The liquid electrolyte (1 M $LiPF_6$ in EC : DEC = 1 : 1 vol%) coin half-cell was tested at C/10 as a reference at room temperature. (c) Discharge capacity retention and coulombic efficiency of the Ge50-based ASSB with wetted Li metal. Measured at a current density of 16 mA g^{-1} (C/10, where 1C = 160 mA g^{-1}) at room temperature.

1.14 mg cm^{-2} (Fig. 7b) to 36.80 mg cm^{-2}, the Ge50-based ASSB still shows good electrochemical activity and reversibility at room temperature. This clearly demonstrates that the co-sintering capability of the Ge-substituted LSPO SE can further increase the energy density by enabling the formation of intimate interfacial contacts between components. Considering the high loading of the thick cathode, an areal capacity of 4.49 mAh cm^{-2} (corresponding to an areal energy density of 16.9 mWh cm^{-2}) was achieved under a current density of 30 μA cm^{-2}. After the co-sintering process, the SE layer can be polished down to ~50 μm, and a thin Li metal layer of about 6 μm can be attached *via* the wetting process (SI Fig. S5). Under these conditions, the volumetric and gravimetric energy densities of the ASSB are calculated to be 841 Wh L^{-1} and 246 Wh kg^{-1}. Detailed component information used for energy density calculations is provided in SI Table S4. These values are remarkably high, even though the active material occupies less than 40 vol% of the cathode composite, indicating the potential to further achieve even higher energy density by increasing the active material fraction. This clearly demonstrates that the Ge50-based ASSB can further enhance its energy density by increasing the thickness of the composite electrode due to the improved Li ionic conductivity, superior co-sintering capability with a high-capacity cathode, and excellent Li metal wettability. In the liquid electrolyte cell, the wetting problem of the viscous electrolyte can easily cause the limited ionic transport in the electrode and thereby the thickness of the electrode in a cell is severely restricted. The capability of the co-sintering process in the LISICON-type oxide-based SEs can enable constructing an ultra-thick composite electrode even without the external pressure in making/operating ASSBs. As a result, using the thick electrode in LISICON-based ASSB can offer significant

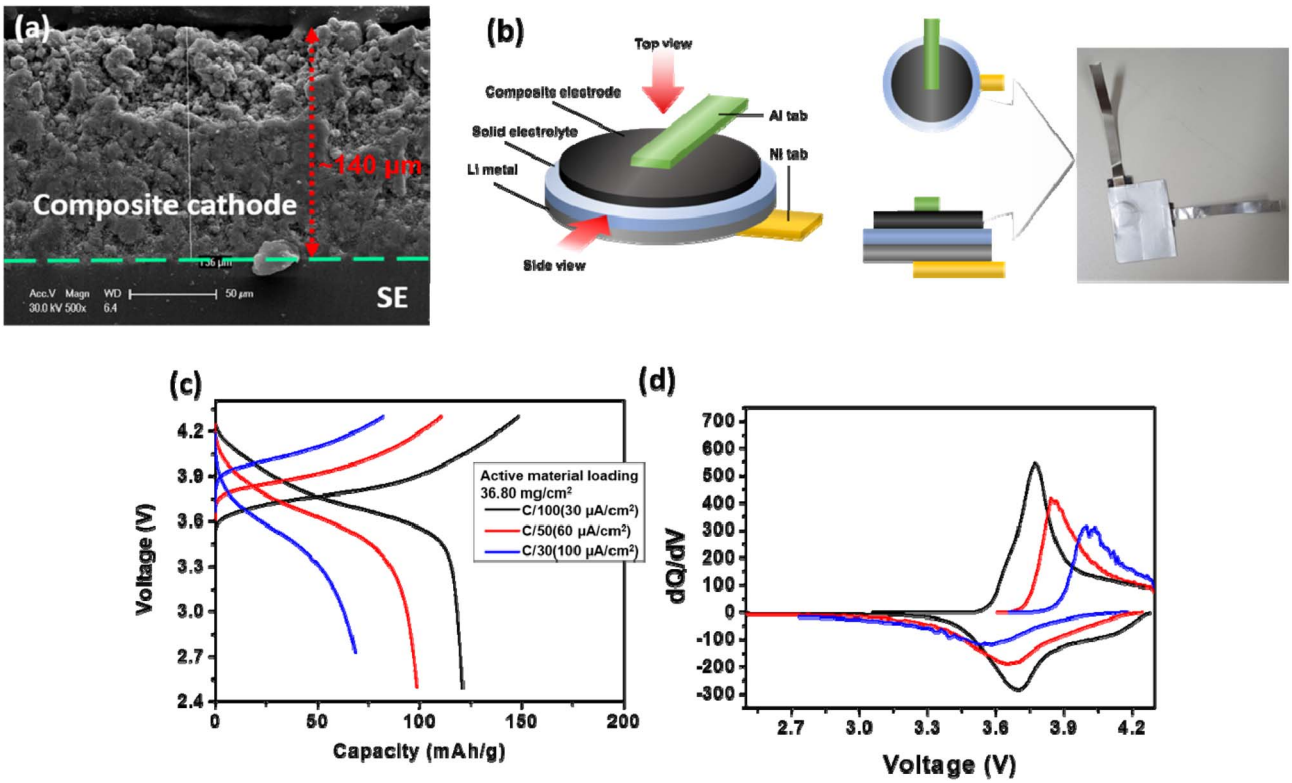

Fig. 8 (a) SEM image of a thick composite electrode_(active material loading density: 36.80 mg cm^{-2} and ~140 μm). (b) Schematic diagram of the Ge50-based ASSB and photo of pouch-type ASSB. (c) Voltage curve and (d) d*Q*/d*V* plot of NCM622| LISICON | Li metal ASSBs with different current densities. In operating the ASSB cell at room temperature, no external pressure is needed.

advantages over cells with liquid electrolytes in addition to the benefit of being free from external pressure during operation, and can provide a totally novel strategy to achieve high energy density in ASSBs unlike the liquid electrolyte cells.

3 Discussion

The poor Li ionic conductivity of the LISICON-type SEs is significantly improved by the substitution of Ge instead of equal amounts of P and Si. The Ge substitution can increase the Li ionic conductivity to 2.5×10^{-5} S cm^{-1}, approximately 5 times higher than that of the bare sample. The incorporation of Ge into the bulk can linearly increase the volume as shown in Fig. 1 because of the large ionic radius of Ge compared to P and Si. The linear increase in the volumes of the Ge substituted samples according to the Ge content indirectly shows that the Ge can be substituted into the bulk structure. Furthermore, the Ge substitution increases the amount of available Li because the P^{5+} ions are replaced by Ge^{4+} ions. The Ge50 sample has 3.75 mol of Li which is much higher than the 3.5 mol of Li in the bare sample. These changes in the Ge-substituted samples substantially increase the poor Li ionic conductivity. The increased Li amount can act as the charge carrier concentration resulting in direct increase in the Li ionic conductivity. Furthermore, the increased Li amount should be incorporated into the two Li sites of the LISICON structure. As a result, the distribution and occupancy of Li into the two Li sites are substantially changed in the Ge-substituted samples (MEM, NMR, and AIMD results). The occupancy of the octahedral Li sites in the Ge-substituted sample is sharply increased because the increased Li can mainly go to the octahedral Li sites in the LISICON structure (NPD and NMR results) even though the bare sample barely has the occupancy of the octahedral Li sites. The increase in the volume of the Ge-substituted samples could affect the distribution of Li between sites possibly because the increased volume can affect the electrostatic interactions. The increase in the occupancy and distribution of Li in the octahedral Li sites significantly improves the continuous Li percolation network between the Li sites (MEM and AIMD simulation). As a result, additional Li percolation pathways can be formed, and the fragmented Li percolation network can be fixed leading to a concerted Li percolation pathway. These topological changes can shorten the hopping distance thereby lowering the percolation threshold and facilitating a long-range Li diffusion. These synergistic effects will increase the Li ionic conductivity in the Ge-substituted samples. Due to the increased Li ionic conductivity, the ASSB with the Ge50 has a reduced polarization and thereby substantially increases the discharge capacity from ~100 mAh g^{-1} to ~150 mAh g^{-1} at room temperature with the same current density compared to the ASSB with LSPO SE.

Furthermore, the Ge-substituted samples have similar superior compatibilities like the LSPO SE which has superior chemical/electrochemical stability with the high-capacity Ni layered oxides and with Li metal even though a large amount of

Ge can be incorporated. The Ge-substituted samples have good chemical stability with the high-capacity Ni-rich layered oxides and thereby, the co-sintering process can be used for constructing all-solid-state cells unlike other oxide-based SEs such as NASICON-type SEs and garnet-type SEs. Surprisingly, the Ge-substituted samples do not undergo any chemical/thermal reactions with melted Li metal resulting in good Li metal wetting behavior even with the Ge element. This is quite different thermal runaway behavior from the Ge substituted NASICON SE such as LAGP. The different Li metal wettability of the Ge substituted samples from the NASICON-type LAGP SE may be due to the presence of Si that can make a lithium alloy or other reaction products. As a result, the Ge-substituted LSPO SE can use a wetted Li metal as an anode. The co-sintering capability of the Ge-substituted SEs with the improved Li ionic conductivity and negligible interfacial resistance can enable the use of the thick composite electrode in making and operating ASSBs without any external pressure. The Ge50-based ASSB with the ~140 μm electrode can deliver high capacity with excellent reversibility leading to high energy density. This clearly demonstrates that the co-sintering capability with high-capacity Ni layered oxides and the improved Li ionic conductivity in the LSPO SE can provide a novel strategy for fabricating a higher energy density ASSB: by depositing an ultra-thick composite electrode layer onto a thin SE with high Li ionic conductivity, it is possible to realize high-energy & cathode-supported ASSBs.

4 Conclusion

Here, the poor Li ionic conductivity of the LISICON-type SE was substantially improved by the substitution of Ge instead of P and Si. The enhancement in the ionic conductivity is ascribed to the effects of the Ge substitution on the available Li amount in the LISICON structure and the occupancy and distribution of Li in Li sites that can increase the connectivity of the Li sites. As a result, continuous Li percolation networks can be additionally created, and the fragmented Li percolation network can be fixed in the LISICON structure. The increased percolation networks substantially enhance the Li ionic conductivity. As a result, the electrochemical activity and kinetics of the ASSB with the Ge-substituted SE can be improved simultaneously. Furthermore, the Ge-substituted LSPO SE still shows superior chemical/electrochemical stability with the Ni-rich layered oxides even at high temperature (>700 °C) and excellent Li metal wettability even with the incorporation of Ge. The co-sintering capability of the Ge-substituted SEs and its enhanced Li ionic conductivity enable the construction of a solid-state cell with an ultra-thick composite electrode without any external pressure. Consequently, the Ge-based ASSB can operate with the thick composite cathode (~140 μm) at room temperature, resulting in substantially increased energy density and reduced polarization owing to the improved Li ionic conductivity. The understanding of the way to increase Li ionic conductivity and the demonstration of high energy density ASSBs *via* thick composite electrodes, which is totally different from conventional approaches, will make LSPO SEs promising candidates for next-generation ASSBs.

5 Methods

5.1 Synthesis of LISICON-type $Li_{3.5}Si_{0.5}P_{0.5}O_4$ (LSPO) & Ge-substituted LSPO, and preparation of sintered pellets

The LSPO and LGSPO solid solutions were synthesized by simple solid-phase reactions in accordance with the target composition $Li_{3.5}Si_{0.5}P_{0.5}O_4$(LSPO), $Li_{3.55}Si_{0.45}P_{0.45}Ge_{0.1}O_4$ (Ge10), $Li_{3.6}Si_{0.4}P_{0.4}Ge_{0.2}O_4$ (Ge20), $Li_{3.65}Si_{0.35}P_{0.35}Ge_{0.3}O_4$ (Ge30), $Li_{3.7}Si_{0.3}P_{0.3}Ge_{0.4}O_4$ (Ge40), and $Li_{3.75}Si_{0.25}P_{0.25}Ge_{0.5}O_4$ (Ge50). Li_2CO_3, SiO_2, $(NH_4)_2HPO_4$, and GeO_2 were stoichiometrically weighed. They were mixed with Zr balls (100 g of 3, 5, and 10 mm diameters) using DI water as a solvent for 24 hours at 300 rpm. After the mixture was dried on a hot plate, it was ground using a mortar. Samples were calcined in an Ar atmosphere at 900 °C to synthesize the target phase and remove volatiles. The synthesized samples were pulverized at 500 rpm for 6 h using a planetary ball-milling machine with Zr balls (1 and 3 mm) with an acetone solvent in a Zr container. The pulverized samples were sieved using a 325 mesh sieve. Then the samples were put into a mold, and pressed at about 300 MPa for 1 minute for making a green body. Sintering was carried out in a tube furnace (TF55035C-1, Lindberg) at 700 °C for 3 hours under oxygen (O_2). Each of 400, 1000, 2000, 3000, and 5000 sandpaper was used to smooth the surface of the sintered pellets.

5.2 Sample characterization

X-ray diffraction (XRD) of the pellet and powder samples was performed by using a Rigaku XRD (D/MAX-2500/PC) with Cu Kα radiation in the 2θ range from 10° to 50° at a rate of 4° min^{-1}. The sintered pellets were crushed using a mortar, and XRD was conducted using this powder. XRD pattern analysis was performed using the X'pert HighScore Plus software program.

Neutron powder diffraction (NPD) data were collected at room temperature on the high-resolution diffractometer Echidna at the OPAL facility (Lucas Heights, Australia) using neutrons of wavelength 1.6220 Å. For the measurements, the samples LSPO, Ge20, Ge40 and Ge50 in the form of ~1 g of powder were loaded in 6 mm diameter cylindrical vanadium cans. Rietveld analysis of the NPD data was performed using the Fullprof Suite with the default neutron scattering lengths. The lattice constants of the samples were evaluated by using Rietveld refinement analysis.

The ionic conductivity of the samples was measured by using EIS without any DC bias, applying an AC amplitude of 0.03 V. For the ASSB full cells, a reduced AC amplitude of 0.01 V was employed to prevent any unintended charging effects. The data of EIS were fitted using Zview2 software. Au paste and Ag paste (P-100, CANS) were applied to both sides of the sintered solid electrolyte pellets as a blocking electrode. The frequency range of the EIS test was from 1 MHz to 0.1 Hz.

Scanning electron microscopy (SEM, XL30 FEG) was performed at the Materials Imaging & Analysis Center of POSCTECH (Pohang, Republic of Korea). Cross-sectional images were obtained at magnifications ranging from ×1000 to ×10

000 to identify the grain size, porosity, and layer thicknesses of the materials used in the ASSB.

X-ray absorption fine structure (XAFS) analysis was conducted on beam line 7D at the Pohang Accelerator Laboratory (Pohang, Republic of Korea). The X-ray absorption near edge structure (XANES) and extended X-ray absorption fine structure (EXAFS) were processed using the IFEFFIT software program. The reference of the Ni K-edge (8333 eV) was taken from Ni metal foil.

5.3 Assembly of the ASSB with Li metal and electrochemical evaluation

The cathode composite electrode for the ASSB was composed of $Li[Ni_{0.6}Co_{0.2}Mn_{0.2}]O_2$, LSPO, Ge-substituted LSPO SE, and Au from the Au paste (TR-1203, TANAKA). Au acts as a conducting agent. In the cathode composite, the volume ratio of the three component materials was 1 : 1 : 1 (Au : NMC : LSPO, Ge-substituted LSPO), determined from the theoretical densities of the materials. The composite cathode slurry was screen-printed on the densely sintered LSPO and Ge-substituted LSPO pellets. In the slurry, Au paste was used as both the screen-printing solution and binder. A circular screen-printing mask with a diameter of 8 mm and a thickness of 120 μm polyimide tape was used. The screen-printed cathode composite on the LSPO, Ge-substituted LSPO SE pellet was co-sintered in a tube furnace at 700 °C for 3 h under an O_2 atmosphere. After that, the opposite surface of the pellet was sequentially polished using sandpapers of 800, 1000, 2000, 3000 and 5000 grit to flatten and smooth the surface, followed by deposition of a 20 nm Au layer *via* sputtering. This interlayer was initially employed to facilitate Li–Au alloying, ensuring a more stable and intimate interface between the SE and Li metal for the baseline characterization (shown in Fig. 7a and b). Subsequently, it was confirmed that a stable interface could be formed without the Au layer; thus, for the tests starting from Fig. 7c, Li metal was directly integrated onto the SE pellet *via* a wetting process at 250 °C. The integrated ASSBs with LSPO, Ge-substituted LSPO SE and Li metal were electrochemically operated at current densities of 4 μA cm^{-2} and 5 μA cm^{-2} at a cutoff voltage window of 4.3–2.5 V at room temperature.

5.4 Fabrication of thick composite electrodes for high-loading ASSBs

Thick composite cathode electrodes were prepared by adopting the screen-printing procedure described above, but with repeated deposition steps. The cathode slurry was screen-printed onto the surface of the sintered Ge50 pellet using a screen-printing mask with diameter 8 mm and a thickness of 120 μm polyimide tape, and dried in an oven at 80 °C for 3 h. Due to solvent evaporation during drying, the thickness decreased to approximately half of the as-printed value. Subsequently, additional depositions were performed on the same area using screen-printing masks of 240 μm and 360 μm thickness to gradually build up the electrode. For each deposition step, the pellet was weighed before and after screen-printing, and the actual amount of active material in the final ASSB was calculated based on the wt% of the active material in the slurry. After the final deposition, the composite cathode layer was densified by heat treatment at 700 °C for 3 h under an O_2 atmosphere. The solid electrolyte surface was polished and the interface with Li metal was formed. Al tab and Ni tab were used as the current collector for the cathode composite and Li metal anode. The resulting pouch-type ASSB was electrochemically operated at current densities of 30, 50, and 100 μA cm^{-2} within a cutoff voltage window of 4.3–2.5 V at room temperature.

5.5 Computational methods

All density functional theory (DFT) calculations were performed within the Vienna *Ab initio* Simulation Package (VASP).[30] The projector-augmented-wave (PAW) method was employed together with the Perdew–Burke–Ernzerhof (PBE)[31] exchange–correlation functional within the generalized gradient approximation (GGA).[32] A plane-wave energy cutoff of 520 eV was used. The convergence criteria for energy and force were 10^{-6} eV and 0.01 eV $Å^{-1}$, respectively. Brillouin-zone integrations used a Γ-centered k-point grid of 2 × 4 × 5, which provides an appropriate sampling density for lattice parameters of approximately $a \approx 11$ Å, $b \approx 6$ Å, and $c \approx 5$ Å. For *ab initio* molecular dynamics (AIMD) simulations, a 1 × 2 × 2 supercell was constructed so that all lattice vectors exceeded 10 Å, and only the Γ point (1 × 1 × 1) was used for Brillouin-zone sampling. The AIMD simulations were carried out within the canonical ensemble (NVT) using a Nosé–Hoover thermostat. The simulation temperatures were set to 1000, 1100, 1200, 1300, and 1400 K in order to obtain temperature-dependent Li-ion diffusion behavior. The time step was set to 2 fs, and the total simulation time at each temperature was 100 ps, including an initial equilibration period of 10 ps. The electronic convergence criterion at each AIMD step was set to 10^{-4} eV.

The diffusion coefficients were obtained from the mean square displacement (MSD) of Li ions based on the Nernst–Einstein equation:

$$\mathrm{MSD}(t) = \frac{1}{N}\sum_{i=1}^{N} |r_i(t+t_0) - r_i(t_0)|^2$$

$$D_{\mathrm{Li}} = \frac{\mathrm{MSD}}{6t} = D^0_{\mathrm{Li}} \exp\left(-\frac{E_a}{k_B T}\right)$$

$$\sigma_{\mathrm{Li}}(T) = \frac{(Z_{\mathrm{Li}}e)^2 N D_{\mathrm{Li}}}{V k_B T}$$

where D^0_{Li} is a pre-factor, k_B is the Boltzmann's constant, T is the simulation temperature, E_a is the activation energy, Z_{Li} is the charge number of Li ion and V is the volume of the simulation box.

The activation energy was extracted by fitting the diffusion coefficients at different temperatures using the Arrhenius equation.

For structural modeling, because the bare and Ge50 structures contain partially occupied Li sites, we enumerated 300 candidate configurations using the pymatgen package.[33] The 20

configurations with the lowest Ewald energies were subsequently relaxed by DFT, and the configuration with the lowest total energy was selected as the final structure. The energies above the convex hull (Ehull) for the most stable Bare and Ge50 configurations are 17.7 meV and 22.0 meV, respectively, indicating thermodynamic stability.

Conflicts of interest

There are no conflicts to declare.

Data availability

The data supporting this article have been included as part of the supplementary information (SI). Supplementary information: SEM images, temperature-dependent ionic conductivity, NPD refinement results, and additional electrochemical data. See DOI: https://doi.org/10.1039/d6ta00467a.

Acknowledgements

This work was supported by the Technology Innovation Program (RS-2023-00254880, Development of cathode active material and current collector for oxide-based MLCB) through the Korea Planning & Evaluation Institute of Industrial Technology (KEIT) funded by the Ministry of Trade, Industry & Energy (MOTIE, Korea).This work was supported by the Technology Innovation Program (RS-2024-00459497, Low-Expansion Mid-Nickel Material for Ultra-Long Cycle Life) through the Korea Planning & Evaluation Institute of Industrial Technology (KEIT) funded by the Ministry of Trade, Industry & Energy (MOTIE, Korea).

References

1 K. Xu, Electrolytes and Interphases in Li-Ion Batteries and Beyond, *Chem. Rev.*, 2014, **114**(23), 11503–11618, DOI: 10.1021/cr500003w.
2 C. Arbizzani, G. Gabrielli and M. Mastragostino, Thermal stability and flammability of electrolytes for lithium-ion batteries, *J. Power Sources*, 2011, **196**(10), 4801–4805, DOI: 10.1016/j.jpowsour.2011.01.068.
3 J. Chen, *et al.*, Research progress and application prospect of solid-state electrolytes in commercial lithium-ion power batteries, *Energy Storage Mater.*, 2021, **35**, 70–87, DOI: 10.1016/j.ensm.2020.11.017.
4 V. Thangadurai, S. Narayanan and D. Pinzaru, Garnet-type solid-state fast Li ion conductors for Li batteries: critical review, *Chem. Soc. Rev.*, 2014, **43**(13), 4714–4727, DOI: 10.1039/C4CS00020J.
5 M. Wakihara, Recent developments in lithium ion batteries, *Mater. Sci. Eng.*, 2001, **33**(4), 109–134, DOI: 10.1016/S0927-796X(01)00030-4.
6 X.-G. Yang, T. Liu and C.-Y. Wang, Thermally modulated lithium iron phosphate batteries for mass-market electric vehicles, *Nat. Energy*, 2021, **6**(2), 176–185, DOI: 10.1038/s41560-020-00757-7.
7 J. C. Bachman, *et al.*, Inorganic Solid-State Electrolytes for Lithium Batteries: Mechanisms and Properties Governing Ion Conduction, *Chem. Rev.*, 2016, **116**(1), 140–162, DOI: 10.1021/acs.chemrev.5b00563.
8 A. Kim, *et al.*, Research Progresses of Garnet-Type Solid Electrolytes for Developing All-Solid-State Li Batteries, *Front. Chem.*, 2020, **8**, 468, DOI: 10.3389/fchem.2020.00468.
9 N. B. Timusheva, *et al.*, Chemical compatibility at the interface of garnet-type Ga-LLZO solid electrolyte and high-energy Li-rich layered oxide cathode for all-solid-state batteries, *Sci. Rep.*, 2025, **15**(1), 241, DOI: 10.1038/s41598-024-78927-w.
10 T. Demuth, *et al.*, Influence of the sintering temperature on LLZO-NCM cathode composites for solid-state batteries studied by transmission electron microscopy, *Matter*, 2023, **6**(7), 2324–2339, DOI: 10.1016/j.matt.2023.04.022.
11 H. Chung and B. Kang, Mechanical and Thermal Failure Induced by Contact between a Li1.5Al0.5Ge1.5(PO4)3 Solid Electrolyte and Li Metal in an All Solid-State Li Cell, *Chem. Mater.*, 2017, **29**(20), 8611–8619, DOI: 10.1021/acs.chemmater.7b02301.
12 F. Ichihara, S. Miyoshi and T. Masuda, Co-sintering process of LiCoO 2 cathodes and NASICON-type LATP solid electrolytes studied by X-ray diffraction and X-ray absorption near edge structure, *Phys. Chem. Chem. Phys.*, 2022, **24**(42), 25878–25884, DOI: 10.1039/D2CP01020H.
13 V. Thangadurai and W. Weppner, Investigations on electrical conductivity and chemical compatibility between fast lithium ion conducting garnet-like Li6BaLa2Ta2O12 and lithium battery cathodes, *J. Power Sources*, 2005, **142**(1), 339–344, DOI: 10.1016/j.jpowsour.2004.11.001.
14 T. Kato, *et al.*, Effects of sintering temperature on interfacial structure and interfacial resistance for all-solid-state rechargeable lithium batteries, *J. Power Sources*, 2016, **325**, 584–590, DOI: 10.1016/j.jpowsour.2016.06.068.
15 H.-S. Kim, *et al.*, Characterization of Sputter-Deposited LiCoO2 Thin Film Grown on NASICON-type Electrolyte for Application in All-Solid-State Rechargeable Lithium Battery, *ACS Appl. Mater. Interfaces*, 2017, **9**(19), 16063–16070, DOI: 10.1021/acsami.6b15305.
16 F. Zhao, *et al.*, Revealing unprecedented cathode interface behavior in all-solid-state batteries with oxychloride solid electrolytes, *Energy Environ. Sci.*, 2024, **17**(12), 4055–4063, DOI: 10.1039/D4EE00750F.
17 Z. Lu, *et al.*, A fluoride-incorporated composite electrolyte enabling high-voltage all-solid-state sulfide-based lithium batteries, *J. Mater. Chem. A*, 2025, **13**(26), 20477–20487, DOI: 10.1039/D5TA03109E.
18 S. Woo and B. Kang, Superior compatibilities of a LISICON-type oxide solid electrolyte enable high energy density all-solid-state batteries, *J. Mater. Chem. A*, 2022, **10**(43), 23185–23194, DOI: 10.1039/D2TA05948G.
19 Y. Deng, *et al.*, Structural and Mechanistic Insights into Fast Lithium-Ion Conduction in Li4SiO4–Li3PO4 Solid Electrolytes, *J. Am. Chem. Soc.*, 2015, **137**(28), 9136–9145, DOI: 10.1021/jacs.5b04444.

20 M. Deng, *et al.*, A Zr–O co-doping strategy for halide solid electrolytes toward high-performance all-solid-state batteries, *J. Mater. Chem. A*, 2025, **13**(38), 32471–32480, DOI: 10.1039/D5TA05447H.
21 L. Ming, *et al.*, Comparative study of oxygen source doping effects on the multidimensional stability of Li5.5PS4.5Cl1.5 solid electrolytes, *J. Mater. Chem. A*, 2026, **14**(18), 10903–10916, DOI: 10.1039/D5TA08492J.
22 K. Suzuki, *et al.*, Synthesis and Electrochemical Properties of Quaternary and Quinary γ-Li3PO4-Type Materials: Effects of Compositional Complexity in Lithium Superionic Conductors, *J. Phys. Chem. C*, 2023, **127**(23), 10947–10952, DOI: 10.1021/acs.jpcc.3c01765.
23 G. Zhao, *et al.*, Extending the frontiers of lithium-ion conducting oxides: development of multicomponent materials with γ-Li3PO4-type structures, *Chem. Mater.*, 2022, **34**(9), 3948–3959, DOI: 10.1021/acs.chemmater.1c04335.
24 G. Zhao, *et al.*, High lithium ionic conductivity of γ-Li3PO4-type solid electrolytes in Li4GeO4– Li4SiO4–Li3VO4 quasi-ternary system, *J. Solid State Chem.*, 2020, **292**, 121651, DOI: 10.1016/j.jssc.2020.121651.
25 Y. Zeng, *et al.*, High-entropy mechanism to boost ionic conductivity, *Science*, 2022, **378**(6626), 1320–1324, DOI: 10.1126/science.abq1346.
26 Y. Wang, *et al.*, Design principles for solid-state lithium superionic conductors, *Nat. Mater.*, 2015, **14**(10), 1026–1031, DOI: 10.1038/nmat4369.
27 R. Koerver, *et al.*, Capacity Fade in Solid-State Batteries: Interphase Formation and Chemomechanical Processes in Nickel-Rich Layered Oxide Cathodes and Lithium Thiophosphate Solid Electrolytes, *Chem. Mater.*, 2017, **29**(13), 5574–5582, DOI: 10.1021/acs.chemmater.7b00931.
28 R. Chen, *et al.*, The Thermal Stability of Lithium Solid Electrolytes with Metallic Lithium, *Joule*, 2020, **4**(4), 812–821, DOI: 10.1016/j.joule.2020.03.012.
29 A. Kim, *et al.*, High Energy Density Ultra-thin Li Metal Solid-State Battery Enabled by a Li2CO3-Proof Garnet-Type Solid Electrolyte, *ACS Energy Lett.*, 2024, **9**(5), 1976–1983, DOI: 10.1021/acsenergylett.4c00217.
30 G. Kresse and J. Furthmüller, Efficiency of ab-initio total energy calculations for metals and semiconductors using a plane-wave basis set, *Comput. Mater. Sci.*, 1996, **6**(1), 15–50, DOI: 10.1016/0927-0256(96)00008-0.
31 G. Kresse and D. Joubert, From ultrasoft pseudopotentials to the projector augmented-wave method, *Phys. Rev. B:Condens. Matter Mater. Phys.*, 1999, **59**(3), 1758–1775, DOI: 10.1103/PhysRevB.59.1758.
32 J. P. Perdew, K. Burke and M. Ernzerhof, Generalized Gradient Approximation Made Simple, *Phys. Rev. Lett.*, 1996, **77**(18), 3865–3868, DOI: 10.1103/PhysRevLett.77.3865.
33 S. P. Ong, *et al.*, Python Materials Genomics (pymatgen): A robust, open-source python library for materials analysis, *Comput. Mater. Sci.*, 2013, **68**, 314–319, DOI: 10.1016/j.commatsci.2012.10.028.

